

1 Vertical variation of optical properties of mixed Asian dust/pollution plumes  
2 according to pathway of air mass transport over East Asia

3  
4 S.-K. Shin<sup>1</sup>, D. Müller<sup>2,a</sup>, Chulkyu Lee<sup>3</sup>, K. H. Lee<sup>4</sup>, D. Shin<sup>5,\*</sup>, Y. J. Kim<sup>1</sup>, Y. M. Noh<sup>6,\*</sup>

5  
6  
7 <sup>1</sup>School of Environmental Science and Engineering, Gwangju Institute of Science &  
8 Technology, Gwangju, Republic of Korea

9 <sup>2</sup>School of Physics, Astronomy and Mathematics, University of Hertfordshire,  
10 Hertfordshire, United Kingdom

11 <sup>3</sup>Korea Meteorological Administration, Seoul, Republic of Korea

12 <sup>4</sup>Department of Atmospheric and Environmental Science, Gangneung-Wonju  
13 National University, Gangneung, Republic of Korea

14 <sup>5</sup>Air Quality Forecasting Centre, Climate and Air Quality Research Department,  
15 National Institute of Environmental Research, Incheon, Republic of Korea

16 <sup>6</sup>International Environmental Research Centre (IERC), Gwangju Institute of Science  
17 & Technology, Gwangju, Republic of Korea

18 <sup>a</sup>formerly at School of Environmental Science and Engineering, Gwangju Institute of  
19 Science & Technology, Gwangju, Republic of Korea

20  
21  
22  
23  
24  
25  
26  
27  
28  
29  
30  
31  
32  
33  
34 \* Corresponding Author

35 Y. M. Noh

36 Tel ) +82-62-715-3392

37 Fax ) +82-62-715-3402

38 Email) [nym@gist.ac.kr](mailto:nym@gist.ac.kr)

39

40 **Abstract:**

41 We use five years (2009 – 2013) of multiwavelength Raman lidar measurements at Gwangju,  
42 Korea (35.10° N, 126.53° E) for the identification of changes of optical properties of East  
43 Asian dust in dependence of its transport path over China. Profiles of backscatter and  
44 extinction coefficients, lidar ratios, and backscatter-related Ångström exponents (wavelength  
45 pair 355/532nm) were measured at Gwangju. Linear particle depolarization ratios were used  
46 to identify East Asian dust layers. We used backward trajectory modelling to identify the  
47 pathway and the vertical position of dust-laden air masses over China during long-range  
48 transport. Most cases of Asian dust events can be described by the emission of dust in desert  
49 areas and subsequent transport over highly polluted regions of China. The Asian dust plumes  
50 could be categorized into two classes according to the height above ground at which these  
51 plumes were transported: (cases I) the dust layers passed over China at high altitude levels (<  
52 3 km) until arrival over Gwangju, and (case II) the Asian dust layers were transported near  
53 the surface and within the lower troposphere (> 3 km) over industrialized areas before they  
54 arrived over Gwangju. We find that the optical characteristics of these mixed Asian dust  
55 layers over Gwangju differ in dependence of their vertical position above ground over China  
56 and the change of height above ground during transport. The mean linear particle  
57 depolarization ratio was  $0.21 \pm 0.06$  (at 532 nm), the mean lidar ratios were  $52 \pm 7$  sr at 355 nm  
58 and  $53 \pm 8$  sr at 532 nm, and the mean Ångström exponent was  $0.74 \pm 0.31$  for case I. In  
59 contrast, plumes transported at lower altitudes (case II) showed low depolarization ratios  
60 ( $0.13 \pm 0.04$  at 532 nm), and higher lidar ratio ( $63 \pm 9$  sr at 355 nm and  $62 \pm 8$  sr at 532 nm) and  
61 Ångström exponents ( $0.98 \pm 0.51$ ). These numbers show that the optical characteristics of  
62 mixed Asian plumes are more similar to optical characteristics of urban pollution. We find a  
63 decrease of the linear depolarization ratio of the mixed dust/pollution plume in dependence of  
64 transport time if the pollution layer travelled over China at low heights, i.e., below  
65 approximately 3 km above ground. In contrast we do not find such a trend if the dust plumes  
66 travelled at heights above 3 km over China. We need a longer time series of lidar  
67 measurements in order to determine in a quantitative way the change of optical properties of  
68 dust with transport time.

69  
70

71 **Key words:** lidar, Asian dust, optical properties, particle depolarization ratio, mixing, vertical  
72 distribution, long-range transport

73 **1. Introduction**

74 Desert dust is the most abundant natural source of atmospheric particles over land. Its  
75 light-absorption capacity is strong in the ultraviolet regions of the solar spectrum (Jacobson  
76 2012). The light-absorption capacity depends on the proportions of  $\text{Fe}_2\text{O}_3$ ,  $\text{Al}_2\text{O}_3$ ,  $\text{SiO}_2$ ,  
77  $\text{CaCO}_3$ ,  $\text{MgCO}_3(\text{s})$ , clays, and other substances. The transport patterns of dust over North  
78 Africa and East Asia as well as the vertical distribution of dust change intra- and inter-  
79 annually. Thus the influence of dust on the atmosphere's radiation balance is complex (Griggs  
80 and Noguera, 2002; Mahowald et al., 2006; Durant et al., 2009). Central East Asia has large  
81 desert regions. Asian dust particles that originate from the Taklamakan desert in west China  
82 and the Gobi desert in Mongolia and northwest China (Figure. 1) influence the regional  
83 climate over East Asia and can be found as far as the west coast of North America (Husar et  
84 al., 2001; McKendry, 2001; Huang et al., 2008). East Asian dust is particularly complicated  
85 as it usually travels over densely populated and highly industrialized areas of China before it  
86 moves out over Pacific Ocean. During transport over East Asia dust mixes with pollutants  
87 such as industrial soot, toxic material, and acidic gases (Sun et al., 2005).

88 Field campaigns, such as ACE-Asia (Huebert et al., 2003) and ADEC (Mikami et al.,  
89 2006) significantly added to our knowledge of the radiative effects of Asian dust. Carrico et  
90 al. (2003) and Yu et al. (2006) found differences of dust optical properties as the result of the  
91 mixing of dust with anthropogenic pollution between source regions of dust and observation  
92 sites downwind of its source regions. The mixing between Asian dust and industrial pollutant  
93 particles has significant influence on the size distribution and the chemical composition of  
94 aerosol plumes (Wang et al., 2007; Sun et al., 2010).

95 There exist few studies on the degree of mixing that occurs between dust and  
96 pollution during transport, the effect of the direction of dust transport across China, and the  
97 vertical distribution of Asian dust layers during long-range transport over China. There still is

98 a lack of understanding of how much of the mixing of dust with pollutants depends on the  
99 vertical distribution of dust when it passes over source regions of anthropogenic pollution in  
100 East Asia. One reason of our limited knowledge is that there are only few vertically-resolved,  
101 long-term observations of pollution over East Asia.

102 LIDAR (LIght Detection And Ranging) is a powerful technique for measuring the  
103 vertical distribution of atmospheric aerosols with high temporal and spatial resolution. In this  
104 study we use Raman lidar data taken at Gwangju, South Korea, between 2009 and 2013. In  
105 our study we focus specifically on lidar observations of Asian dust layers as they passed over  
106 China. We use backward trajectory analysis with HYSPLIT (HYbrid Single Particle  
107 Lagrangian Integrated Trajectory) (Draxler and Rolph, 2003) model to identify the transport  
108 pathway and the vertical distribution of the Asian dust layers during long-range transport.

109 The main objective of this study is to investigate the variation of optical properties of  
110 mixtures of Asian dust with anthropogenic pollution in dependence of the pathways and  
111 vertical distributions of these mixed dust layers during long-range transport. In this  
112 contribution we used the linear particle depolarization ratio to identify these dust layers. We  
113 present vertically-resolved optical properties such as lidar ratio and Ångström exponent.

114 Section 2 presents the methods used in this study. Section 3 presents our results. We  
115 discuss our results and summarize our findings in section 4.

116

## 117 **2. Methodology**

### 118 **2.1 GIST Multi-wavelength Raman lidar**

119 The lidar station, dubbed MRS.LEA (Multi-wavelength Raman Spectrometer Lidar  
120 in East Asia) of the Gwangju Institute of Science and Technology (GIST) is located at 35.10°  
121 N, 126.53° E in the west-south-western part of the Korean peninsula (Figure. 1).

122 A description of the lidar system is given by Noh et al. (2007, 2008). The light source

123 of the lidar is a pulsed Nd:YAG laser that emits light pulses at 355 nm, 532 nm, and 1064 nm.  
124 The laser output power is 140, 154, and 640 mJ at the three emission wavelengths,  
125 respectively. The pulse repetition rate is 10 Hz. We use a beam expander at 532 nm and 1064  
126 nm in order to reduce the divergence of the emitted light. The receiver consists of a 14-inch  
127 Schmidt-Cassegrain telescope. The signals collected by the receiver telescope are separated  
128 according to wavelength with beam splitters and then transmitted to photomultiplier tubes  
129 (PMT). Transient recorders with 12-bit analog-to-digital converters and 250-MHz photon  
130 counters are used for processing the output signals of the PMTs. The system allows us to  
131 retrieve vertical profiles of the particle backscatter coefficients at 355, 532, and 1064 nm, the  
132 particle extinction coefficients at 355 and 532 nm, the linear particle depolarization ratio at  
133 532 nm, the water-vapor mixing-ratio, and profiles of silicon-dioxide (Müller et al., 2010;  
134 Tatarov et al., 2011). Profiles of silicon-dioxide (quartz) can be used as a proxy of the  
135 concentration of mineral dust. In this contribution we use the signals needed for measuring  
136 particle backscatter and extinction coefficients at 355 and 532 nm and the linear particle  
137 depolarization ratio at 532 nm. The measurements were carried out at night time under cloud-  
138 free conditions.

139 The profiles of particle backscatter coefficients ( $\beta_p$ ) at 355 and 532 nm were  
140 calculated with the Raman method (Ansmann et al., 1992b). The overlap effect which  
141 describes the incomplete overlap between outgoing laser beam and field of view of the  
142 receiver telescope is cancelled out for the case of profiles of the backscatter coefficient  
143 because the ratios of two signals (elastic signals from particles and molecules and the  
144 nitrogen Raman signals) are computed (Wandinger and Ansmann, 2002). In that way we can  
145 retrieve vertical profiles of the backscatter coefficient to 400 m above ground. The vertical  
146 profiles of the aerosol extinction coefficients ( $\alpha_p$ ) at 355 and 532 nm were derived with the  
147 use of the nitrogen vibration Raman signals at 387 and 607 nm (Ansmann et al., 1990),

148 respectively. The aerosol extinction coefficients can be retrieved above 780 m and 540 m  
149 above ground at the measurement wavelengths of 355 nm and 532 nm, respectively. We  
150 derive particle extinction-to-backscatter ratios (lidar ratios, denoted as  $S$  in this contribution)  
151 at 355 and 532 nm from the profiles of  $\beta_p$  and  $\alpha_p$ . The lidar ratios can be used for aerosol  
152 typing (Müller et al., 2007). Murayama et al., (2004) find values of  $S = 48.6$  sr at 355 nm and  
153  $S = 43.1$  sr at 532 in a well-isolated Gobi dust-laden layer observed above 4 km over Tokyo.  
154 De Tomasi et al. (2003) report an  $S$  value less than 50 sr at 351 nm for a Saharan dust layer.  
155 Values of  $S$  at 355 nm ranged between 50 sr and 80 sr for dust observed over Leipzig,  
156 Germany (Mattis et al., 2002). In contrast, Ferrare et al. (2002) report a high value of  $68 \pm 12$   
157 sr of the lidar ratio at 355 nm. This high lidar ratio was associated with air masses advected  
158 from urban/industrial areas. Omar et al. (2009) finds values of 65-70 sr for the lidar ratio at  
159 532 nm. The numbers describe continental-polluted aerosols and polluted dust.

160 The backscatter-related Ångström exponent for the wavelength pair of 355/532 nm  
161 (denoted as  $\mathring{A}_\beta$ ) is computed, too. The backscatter-related Ångström exponent is a good  
162 indicator of the size of particles. High values ( $>1$ ) are typically observed for accumulation  
163 mode particles such as fresh biomass-burning particles. Low values ( $\sim 0$ ) are observed for  
164 coarse mode particles such as Saharan dust or Asian dust (Eck et al., 1999; Sakai et al., 2002,  
165 Chen et al., 2007). The values of 0.2-0.3 are reported as the values of  $\mathring{A}_\beta$  for Saharan dust  
166 (Murayama et al., 2002; Tesche et al., 2009). Chen et al. (2007) and Müller et al. (2010) find  
167 values of 0.7-1.5 for  $\mathring{A}_\beta$  for a mixture of mineral dust with urban haze. Values of 0.8-1.4 for  
168  $\mathring{A}_\beta$  were found for heavily polluted continental aerosol layers (Franke et al., 2003).

169 The depolarization ratio is used as indicator of particle shape (Bohren and Huffman,  
170 1983). High values of the depolarization ratio of 0.3 to 0.35 at 532 nm indicate nearly pure  
171 dust (Sugimoto and Lee, 2006; Freudenthaler et al., 2009). For example, Freudenthaler et al.  
172 (2009) report a value of  $\delta_p = 0.31$  at 532 nm for Saharan dust observed during SAMUM 2006.

173 Lidar observations were carried out close to the Taklamakan desert (Iwasaka et al., 2003) and  
174 the Gobi desert (Yi et al., 2014). We assume that these dust layers exhibit nearly pure dust  
175 conditions as anthropogenic pollution sources in these isolated areas are sparse. Values of  $\delta_p$   
176 are in the range of 0.3 to 0.35 at 532 nm (Iwasaka et al., 2003; Yi et al., 2014). Small values,  
177 e.g., values from 0.08 to 0.1 usually are an indicator that dust is mixed with spherical  
178 particles (Murayama et al., 2004; Chen et al., 2009; Tesche et al., 2009; Burton et al., 2013).  
179 Anthropogenic aerosols normally are spherical with a small depolarization ratio (Murayama  
180 et al., 2003). The degree of depolarization decreases as the sphericity of particles increases.  
181 The depolarization ratio is dependent on the mixing ratio of dust with spherical particles. For  
182 instance, Burton et al. (2013) report values of  $\delta_p = 0.13-0.20$  and  $0.03-0.07$  at 532 nm for  
183 polluted dust and urban aerosol particles, respectively.

184 Parallel polarized and perpendicular polarized signals are measured at 532 nm. The  
185 linear volume depolarization ratio (aerosols + molecules)  $\delta$  is defined as

$$186 \quad \delta = \frac{P_{\perp}}{P_{\parallel} + P_{\perp}}. \quad (1)$$

187  $P_{\perp}$  and  $P_{\parallel}$  denote the backscatter signal intensities that are polarized perpendicular  
188 and parallel with respect to the plane of polarization of the emitted laser beam, respectively.  
189 The  $\delta$  can be also defined as  $P_{\perp}/P_{\parallel}$  (Cairo et al., 1999). We calculated the  $\delta$  by using both  
190 definitions and compared the difference between the derived values. The results from each  
191 individual definition agree within the uncertainty of our depolarization ratio measurements  
192 (Tesche et al., 2009; Shin et al., 2013).

193 The linear particle depolarization ratio  $\delta_p$  differs from  $\delta$  as it depends on the  
194 concentration of particles in relation to the concentration of air molecules. In this contribution  
195 we use the linear particle depolarization ratio ( $\delta_p$ ) according to the definition by Shimizu et al.  
196 (2004):

197 
$$\delta_p = \frac{\delta(z)R_B(z) - \delta_m}{R_B(z) - 1}. \quad (2)$$

198 The term  $\delta_m$  is the linear depolarization ratio of air molecules at the wavelength of  
 199 the emitted laser wavelength. We used the value  $\delta_m=0.0044$  (Behrendt and Nakamura, 2002).  
 200 This value takes account of our interference filters which have a full width at half maximum  
 201 of 1.0 nm.  $R_B(z)$  is the backscatter ratio, expressed as  $(\beta_p + \beta_m)/\beta_m$  at altitude  $z$ .  $\beta_m$  denotes the  
 202 backscatter coefficient of atmospheric molecules. The calibration of the polarization channels  
 203 was carried out by using rotating polarizers following the methodology explained by  
 204 Freudenthaler et al. (2009).

205

## 206 **2.2 Dust Layer Identification**

207 We use the profiles of the linear particle depolarization ratio for the identification of  
 208 the Asian dust layers. An example of how the Asian dust layer was determined is shown in  
 209 Figure 2. The Asian dust plume reached Korea on 22 April 2012. Figure 2 shows the time-  
 210 height cross section of the range-corrected backscatter signals and the linear volume  
 211 depolarization ratio at 532 nm. Figure 2 also shows the mean profiles of  $\delta$  and  $\delta_p$ ,  $S$  at 355  
 212 and 532 nm, and  $\hat{A}_\beta$  for the measurement from 13:15 to 14:05 UTC.

213 Values of  $\delta_p$  for individual aerosol types are reported in literature, e.g.  $\delta_p$  for Asian  
 214 dust particles varies from 0.08-0.35 (Murayama et al., 2004; Shimizu et al., 2004; Chen et al.,  
 215 2009; Shin et al., 2013) at 532 nm. Asian dust generally mixes with pollution during long-  
 216 range transport which leads to variable  $\delta_p$ . Thus, this range of 0.08-0.35 likely describes  
 217 mixtures of dust with anthropogenic pollution. For instance, Chen et al. (2009) uses 0.08 as  
 218 threshold value to identify dust in pollution. Furthermore, optical properties may also change  
 219 during long-range transport. Shimizu et al. (2004) define 0.1 as threshold value for the  
 220 determination of polluted dust. In this study we used 0.08 as threshold value of  $\delta_p$  to identify



221 dust.

222 In figure 2, the layer between 2.7 km 4.6 km (layer II) contains Asian dust particles  
223 as suggested from the values of  $\delta_p$ , which are higher than 0.16. The mean value of  $\delta_p$  in the  
224 layer between 1.2 km and 2.5 km (layer I) is 0.11 and thus also points to the presence of dust  
225 particles though the concentration of dust particles compared to the concentration of particles  
226 of anthropogenic pollution may be lower in layer I compared to layer II.

227 Other aerosol optical properties in layer I and layer II differ, too. The values of the  $S$   
228 in layer I are  $64 \pm 4$  sr and  $66 \pm 4$  sr at 355 and 532 nm, respectively. The values of the  $S$  in  
229 layer II are as low  $55 \pm 4$  sr and  $55 \pm 3$  sr at 355 and 532 nm, respectively, see Fig. 2d. The  
230 standard deviations were computed for the lidar ratios in each of the layers we could identify.

231 The values of  $\mathring{A}_\beta$  in layer I are  $\sim 0.93$  and thus considerably higher than in layer II  
232 where we find a value of  $\sim 0.42$ . These numbers suggest that the concentration of small  
233 particles is higher in layer I than in layer II, respectively that the mean size of particles in  
234 layer I is smaller than the mean size of particles in layer II. Regarding the interpretation of the  
235 numbers of  $\mathring{A}_\beta$  we need to keep in mind that the backscatter-related Ångström exponent not  
236 only depends on particle size but also on the complex refractive index and particle shape. The  
237 same holds true for the values of  $S$ . The different numbers thus could also result from  
238 differences in particle shape and their absorption properties in these mixed Asian dust layers.

239

### 240 **2.3 Analysis of Backward Trajectories and Model Simulations of Pollution Emissions**

241 We used the HYSPLIT model (Draxler and Rolph, 2003) to generate 120 hours  
242 backward trajectories for air parcels arriving above our lidar site. The trajectories describe the  
243 different altitude levels in which dust was transported prior to the lidar observations. They  
244 also allow us to trace back the origin of the dust layers and the transport path.

245 The Monitoring Atmospheric Composition and Climate (MACC) global air quality

246 service of the European Centre for Medium-Range Weather Forecasts (ECMWF) provides a  
247 re-analysis of global atmospheric composition. The re-analysis assimilates satellite data, e.g.  
248 total aerosol optical depth (AOD) which is provided by the Moderate Resolution Imaging  
249 Spectroradiometer (MODIS), into a global model and data assimilation system to correct for  
250 model departures from observational data (Bellouin et al., 2013; Inness et al., 2013). This re-  
251 analysis provides fields of aerosols, namely mineral dust, black carbon, organic matter, and  
252 sulphate, as well as chemically reactive gases, and greenhouse gases. We used the aerosol  
253 AOD from the MACC re-analysis to determine the intensity of pollution (AOD) in densely  
254 populated and industrialized regions along the transport path of the dust layers and to  
255 investigate the influence of anthropogenic pollution particles on the variation of the optical  
256 properties of Asian dust.

257

### 258 **3. Results and discussion**

259 We present data that cover the time from 2009-2013. During this time we observed  
260 38 Asian dust layers on 32 days. These Asian dust layers were identified on the basis of the  
261 linear particle depolarization ratio measurements as described in section 2.2. The vertical  
262 profiles of the linear particle depolarization ratio allow us to determine the vertical  
263 distribution of the Asian dust layers.

264 Figure 3 shows the frequency distribution of  $\delta_p$ ,  $S$ , and  $\dot{A}_\beta$  of Asian dust plumes  
265 observed during the observation period. The average value of  $\delta_p$  for all observed Asian dust  
266 layers is  $0.17 \pm 0.02$ . The average values of  $S$  are  $57 \pm 6$  sr at 355 nm and  $57 \pm 7$  sr at 532 nm.  
267 The mean value of  $\dot{A}_\beta$  is  $0.84 \pm 0.37$ . The optical properties of each individual Asian dust layer  
268 vary over a wide range of values. We find values of 0.08-0.33 for  $\delta_p$ , 38-83 sr for  $S$  at 355 nm,  
269 41-73 sr for  $S$  at 532 nm, and 0.38-1.71 for  $\dot{A}_\beta$ . The maximum value of  $\delta_p$  is 0.33 at 532 nm.  
270 The minimum values of  $S$  at 355 nm and 532 nm are 38 sr and 41 sr, respectively. The

271 minimum value of  $\dot{A}_\beta$  is 0.38. This maximum value of  $\delta_p$  and the minimum values of  $S$  at 355  
272 nm and 532 nm and  $\dot{A}_\beta$  are similar to the values of optical properties for pure dust particles.  
273 In contrast with these values, low values of  $\delta_p$  and high values of  $S$  and  $\dot{A}_\beta$  are also measured.  
274 We find that the minimum value of  $\delta_p$  is 0.08 at 532 nm. The maximum values of  $S$  at 355  
275 nm and 532 nm are 83 sr and 73 sr, respectively. The maximum value of  $\dot{A}_\beta$  is 1.71. These  
276 values are remarkably different from the values of optical properties of pure dust.

277 We speculate that these differences of the values of the optical properties of dust  
278 particles are caused by the effect of long-range transport during which dust mixes with  
279 anthropogenic pollution or biomass burning smoke when passing over industrialized/densely  
280 populated regions in China.

281

### 282 **3.1 Qualitative Analysis of the Variation of Optical Properties of Mixed-Dust in** 283 **Dependence of Pollution Levels**

284 We divided the dust layers into two episodes. The two episodes differ according to  
285 the level of pollution emissions along the transport pathway of the dust plumes. The  
286 separation of our measurements into these two episodes was done on the basis of the  
287 distribution of aerosol optical depth (AOD) of anthropogenic pollution over China. The  
288 Asian dust layers were classified as “more polluted”, i.e., “MP” Asian dust when the  
289 modelled AOD of anthropogenic pollution on that day was higher than the average AOD  
290 (modelled) of all 32 observation days considered in this study. In contrast, Asian dust layers  
291 that passed over China during episodes of lower AOD, i.e., AOD was below the mean value  
292 of modelled AOD of all 32 observation days, are denoted as “less polluted”, i.e., “LP” Asian  
293 dust.

294 We used model results by MACC and backward trajectory analysis (see section 2.3)  
295 for the interpretation of our lidar results as we do not have direct observations of pollution,

296 e.g. particle optical depth, lidar ratios, the linear particle depolarization ratios, and Ångström  
297 exponents along the transport path of the pollution plumes. The reliability of inferring AOD  
298 of pollution from MACC re-analysis is validated by comparing it to results from AERONET  
299 sunphotometer measurements. MACC model is widely used to estimate AOD of pollution  
300 (Bellouin et al., 2013; Cesnulyte et al., 2014).

301 Figure 4 shows the distribution of aerosol optical depth (AOD) at 550 nm for dust  
302 and anthropogenic pollution on 10 April 2010 and 8 March 2013. These pollutants include  
303 organic matter, black carbon, and sulphate aerosol. The pollution AOD was computed with  
304 the MACC model using re-analysis data of ECMWF. The re-analysis data from the MACC  
305 model can be downloaded at the web page of ECMWF  
306 (<http://apps.ecmwf.int/datasets/data/macc-reanalysis/>). Fig. 4 shows that Asian dust particles  
307 emitted from the Taklamakan and the Gobi desert were transported across China. The model  
308 results of AOD of anthropogenic pollutants over China for 10 April 2010 are significantly  
309 higher than the model results of AOD on 8 March 2013.

310 Figure 5 shows the scatter diagram of  $\mathring{A}_\beta$  and  $S$  at 355 nm and 532 nm versus  $\delta_p$  in  
311 dependence of the transport events denoted as MP and LP. The mean value of  $\delta_p$  of the Asian  
312 dust layers denoted as “LP” cases ranges between 0.08 (threshold value that we use to  
313 identify dust) and 0.33. The corresponding values of  $\mathring{A}_\beta$  vary between 0.38 and 1.71. The  
314 lidar ratios range between 38 sr and 83 sr at 355 nm and between 41 sr and 73 sr at 532 nm.  
315 The negative correlation of  $\delta_p$  with  $\mathring{A}_\beta$  indicates that the impact of the non-spherical particles  
316 (Asian dust with high  $\delta_p$ ) on the backscattered light decreases with increasing  $\mathring{A}_\beta$ . Higher  
317 values of  $\mathring{A}_\beta$  indicate a considerable concentration of anthropogenic pollution particles which  
318 in turn results in lower values of  $\delta_p$ , of the mixed dust/pollution plumes.

319 Lower values of  $\delta_p$  are dominantly found in the domain where lidar ratios are above  
320 60-70 sr, except for a few cases. Comparably high lidar ratios are associated with air masses

321 from urban/industrial areas (Noh et al., 2007; Müller et al., 2007; Burton et al., 2012). We  
322 find high values of  $\delta_p$  for lidar ratios of  $57 \pm 7$  sr at 355 nm and  $55 \pm 7$  sr at 532 nm.

323 With regard to the MP cases the mean  $\delta_p$  varies from 0.08 to 0.30. The corresponding  
324 values of  $\dot{A}_\beta$  vary between 0.42 and 1.56. The lidar ratios vary between 44 sr and 74 sr at  
325 355 nm and between 48 sr and 72 sr at 532 nm, respectively.

326 Figure 5(d-f) shows a negative correlation of  $\delta_p$  with  $\dot{A}_\beta$  and  $S$  at 355 nm and 532 nm.  
327 The mean values of the LP and MP cases are summarized in table 1. The transport pathway of  
328 dust over eastern China should influence the degree to which anthropogenic aerosols in the  
329 industrial areas contribute to the change of optical properties of dust. However, we do not  
330 find significant differences between the LP cases and MP cases. We assume that there is  
331 another factor that influences the change of the optical properties of the dust layers we  
332 observed.

333

### 334 **3.2 Influence of pathway and vertical distribution of anthropogenic pollution on optical** 335 **properties of Asian dust**

336 We classified the Asian dust plumes into 2 categories with regard to height above  
337 ground when they passed over regions of anthropogenic emissions. We used 3 km height  
338 above ground for the classification. The height of 3 km is reported as the planetary boundary  
339 layer. Pollutants emitted at the surface predominantly stay in the planetary boundary layer  
340 (Noh et al., 2007; Xie et al., 2015). We assume that height above ground influences how  
341 much anthropogenic pollution may mix with the dust layers and thus changes the optical  
342 properties of the dust layers. The vertical positions of the dust plumes above ground during  
343 transport over China were inferred from the model results. We assume that the height of the  
344 dust plumes above ground can be distinguished by HYSPLIT model results although the  
345 results may have a certain error because of the spatial and temporal complexity of the

346 meteorological fields involved in the computations.

347 Figure 6 shows the transport pathway and the change of the vertical position of the  
348 dust plumes during transport to our lidar site. It is clear that backward trajectories cannot  
349 provide us with information on the concentration of dust and anthropogenic pollution in the  
350 air masses prior to observation over Korea. Still, backward trajectories show if the air masses  
351 originated from or nearby the desert regions, and whether the air masses passed over densely  
352 populated/industrialized regions.

353 Case I includes those Asian dust plumes that passed over industrialized areas in  
354 China at high altitude level ( $> 3\text{km}$  height above ground) as shown in figure 6a. The Asian  
355 dust plumes were classified as Case II when they were transported through the near  
356 surface/lower troposphere ( $< 3\text{km}$  height above ground) over industrialized areas in China,  
357 i.e., longitude range between  $110^\circ \text{ E}$  and  $125^\circ \text{ E}$ ; the locations of industrialized and densely  
358 populated regions in China are shown in figure 1.

359 The mean values of the linear particle depolarization ratios of the Asian dust plumes  
360 we observed are lower compared to the linear particle depolarization ratios of pure dust  
361 particles. For example, Freudenthaler et al. (2009) report a value of  $\delta_p = 0.31$  at 532 nm for  
362 pure Saharan dust observed during SAMUM 2006.

363 The values of  $\delta_p$  and the corresponding values of  $\mathring{A}_\beta$  and  $S$  at 355 nm and 532 nm for  
364 the cases I and II are also shown in figure 6. The corresponding mean values of the  
365 parameters of these two cases are also summarized in table 1.

366 We find different clusters of the optical properties of the dust layers when we take  
367 into consideration their vertical position during transport. The cases I show larger values of  $\delta_p$   
368 compared to the depolarization ratios in cases II. On average,  $\mathring{A}_\beta$  of case I is smaller than  $\mathring{A}_\beta$   
369 of case II. The average values of  $\delta_p$  and  $\mathring{A}_\beta$  are  $0.21 \pm 0.06$  and  $0.74 \pm 0.31$ , respectively, for  
370 case I. In contrast,  $\delta_p$  and  $\mathring{A}_\beta$  are  $0.13 \pm 0.04$  and  $0.98 \pm 0.35$ , respectively, for case II. The

371 lowest values of  $S$  at 355 nm and 532 nm are also measured for high values of  $\delta_p$  ( $0.21 \pm 0.06$ ).  
372 We find values of  $52 \pm 7$  sr at 355 nm and  $53 \pm 8$  sr at 532 nm, respectively, for case I.  
373 Comparably high values of  $S$  were found for case II, i.e.  $63 \pm 9$  sr at 355 nm and  $62 \pm 8$  sr at  
374 532 nm. In that case the value of  $\delta_p$  is  $0.13 \pm 0.04$ .

375 There are several previous studies that report on linear particle depolarization ratios  
376 of polluted dust after long-range transport. According to these studies the observed dust  
377 particles were partly/completely mixed with anthropogenic pollution (Sakai et al., 2002;  
378 Müller et al., 2003; Shimizu et al., 2004; Chen et al., 2007). As a result of the mixing of dust  
379 with anthropogenic pollution, the values of  $\delta_p$  were lower than the values of pure dust, which  
380 is estimated to be 0.3-0.35 (Murayama et al., 2004; Freudenthaler et al., 2009). Likewise, the  
381 values of  $\dot{A}_\beta$  and  $S$  also differ compared to the values of  $\dot{A}_\beta$  and  $S$  of pure dust.

382 We assume that the dust particles carried more anthropogenic pollution in cases  
383 where the air masses travelled near the surface. Consequently, the optical characteristics of  
384 the dust/pollution layers of case II are dominated by the optical properties of anthropogenic  
385 pollutants. In contrast, the optical properties of dust layers that travelled at high altitudes  
386 (case I) are less influenced by urban/industrial pollutants. Thus, the optical properties of these  
387 dust layers are more likely to be those of pure dust.

388 The Asian dust plumes were classified into 4 categories. We considered not only the  
389 level of pollution emissions along the transport pathway, i.e., “MP” Asian dust and “LP”  
390 Asian dust, but also the vertical position of the layers when they passed over polluted regions  
391 of China (“below 3km” and “above 3km”). Figure 7 shows scatter diagrams of  $\dot{A}_\beta$   
392 (wavelength range 355/532 nm), and  $S$  at 355 nm and 532 nm versus  $\delta_p$  at 532 nm in  
393 dependence of the level of pollution emission and the vertical position. The corresponding  
394 mean values of the optical parameters of those clusters are given in Table 1. We expect that  
395 the optical properties of Asian dust change most if pollution levels (in terms of AOD) are

396 high, (MP Asian case) and when the corresponding air masses passed over industrialized area  
397 of China at low altitude (below 3km height above ground). The mean values of  $\delta_p$  at 532 nm  
398 and  $\mathring{A}_\beta$  are  $0.13\pm 0.04$  and  $1.09\pm 0.30$ , respectively, for this case which is denoted as  
399 “MP\_below 3km”. The mean values of  $S$  are  $61\pm 10$  sr at 355 nm and  $64\pm 7$  sr at 532 nm.  
400 However, these values of optical properties of dust for MP\_below 3km are not significantly  
401 different from the case of “LP\_below 3km”. In that case the mean values of  $\delta_p$  at 532 nm and  
402  $\mathring{A}_\beta$  are  $0.13\pm 0.03$  and  $1.00\pm 0.38$ , respectively. The mean values of  $S$  are  $64\pm 9$  sr at 355 nm and  
403  $62\pm 8$  sr at 532 nm.

404 The values of optical properties between “MP” and “LP” at high altitude also do not  
405 differ significantly. The mean values of  $\delta_p$  at 532 nm,  $\mathring{A}_\beta$ , and  $S$  are  $0.24\pm 0.05$ ,  $0.58\pm 0.14$ , and  
406  $53\pm 5$  sr at 355 nm and  $53\pm 2$  sr at 532 nm, respectively, for the case “MP\_above 3km”. The  
407 highest values of  $\delta_p$  and lowest values of  $\mathring{A}_\beta$  are found for this case.

408 In the case of “LP\_above 3km” the mean values of  $\delta_p$  at 532 nm and  $\mathring{A}_\beta$  are  
409  $0.21\pm 0.05$  and  $0.65\pm 0.20$ , respectively. The mean values of  $S$  are  $51\pm 8$  sr at 355 nm and  $49\pm 9$  sr,  
410 respectively. We believe that the changes in the optical properties of Asian dust depend on the  
411 vertical position of the dust plume rather than the level of pollution emission during transport.

412 The clusters denoted as Case I and Case II were classified according to the altitude  
413 (above ground) at which the dust-laden air masses passed over industrialized/populated  
414 regions of China. The differences of the optical properties of the dust layers are shown in  
415 figure 8. The corresponding values of the optical characteristics of the Asian dust layers at  
416 each individual height are summarized in table 2. The difference of the optical characteristics  
417 of East Asian dust layers that travelled in surface-near heights and at high altitudes is obvious.  
418 The values of  $\delta_p$ ,  $\mathring{A}_\beta$ , and  $S$  are  $0.12\pm 0.01$ ,  $1.00\pm 0.43$ , and  $63\pm 7$  sr at 355 nm and  $64\pm 6$  sr at  
419 532 nm, respectively, when Asian dust passed over China below 1 km height above ground.  
420 These values reflect the fact that the optical properties of the dust/pollution plumes are



421 dominated by the anthropogenic part of the particles in these plumes. Lower values of  $\delta_p$   
422 represent the dominance of spherical particles, i.e. the presence of urban pollution. High  
423 values of  $\mathring{A}_\beta$  indicate that small particles dominate in the lower altitude level. The high lidar  
424 ratio also indicates the presence of urban pollution which tends to be more light-absorbing  
425 (Müller et al., 2007). In contrast, values for  $\delta_p$ ,  $\mathring{A}_\beta$ , and  $S$  are  $0.23\pm 0.04$ ,  $0.60\pm 0.17$ , and  $50\pm 6$   
426 sr at 355 nm and  $49\pm 5$  sr at 532 nm, respectively, after the dust layers had passed over China  
427 at high altitudes, i.e., above 3 km. These values more likely reflect the optical characteristic  
428 of Asian dust particles that are less affected by the contribution of anthropogenic pollution.  
429 The optical properties of Asian dust layer observed in our study reflect mixtures between  
430 different aerosol types.

431 We notice that these variations of the optical properties of Asian dust layers may not  
432 only result from external mixing. Hygroscopic growth, aging and deposition during transport,  
433 and internal mixing might be also affect dust properties (Burton et al., 2014). The  
434 interpretation of the mixing state of Asian dust is a challenging task. The mixing state  
435 depends on many variables which are poorly known. Sugimoto et al. (2015) tried to identify  
436 the mixing state of Asian dust (internal mixing or external mixing) by using analytical  
437 relationships inferred from lidar observation. However, we will not go into details here. We  
438 assume that most of the Asian dust observed in this study was externally mixed.

439 The altitude in which the Asian dust layers passed over China have significant  
440 influence on their optical characteristics. In our study, we took 3 km above ground as  
441 threshold value as we observed a notable change of optical properties of the dust/pollution  
442 plumes if they travelled above or below 3 km height above ground. Pollution particles below  
443 3 km could mix and interact with Asian dust particles (more influence). In contrast, we  
444 assume that optical properties of dust particles above 3 km are not that much influenced by  
445 anthropogenic pollution as the mixing of pollution into these heights is less intense.

446 We emphasize that this threshold value of 3 km is merely a best estimate which is  
447 governed by the set of data we have at hand. We lack in additional information that would  
448 allow us to refine our data analysis. For example a longer time series of lidar measurements,  
449 (vertically resolved) observations of pollution transported over China, measurements under  
450 much more variable meteorological conditions, additional modelling results, just to name a  
451 few reasons, might change this threshold value.

452 We also investigated the optical properties of Asian dust with respect to transport  
453 time at different height level. Figure 9 shows scatter diagrams of optical properties of Asian  
454 dust versus the transport time. The correlation study is based on HYSPLIT model results, our  
455 profiles of  $\delta_p$ ,  $\dot{A}_\beta$ , and  $S$ , and the time (in hours) the Asian dust spent in polluted regions over  
456 China during the transport. We can only use HYSPLIT results as an estimate of the total  
457 transport time and the time the plumes spent over pollution regions of China. The total  
458 transport time may have considerable uncertainty. We need to decide from the trajectories the  
459 start point of dust emission and this means we take the time when the air parcel (defined by  
460 its trajectory) left one of the desert regions in Central Asia. The height above ground during  
461 transport and the time the plumes spent over pollution regions also contains uncertainty as we  
462 neither have direct measurements of the height distribution of the plumes over China during  
463 transport nor do we have information on the pollution levels over China while the desert  
464 plumes travelled over China in the various height layers. We can merely assume that the  
465 likelihood of mixing with dust and pollution increases the lower the dust travels above  
466 ground and the longer it travels at low heights.

467 We again used our classification of Case I and Case II. However, we refined the  
468 vertical resolution to 5 height layers, i.e. transport occurred below 1 km, from 1-2 km, from  
469 2-3 km, from 3-4 km, and above 4 km. We wanted to test if a more refined height separation  
470 would give us more insight on the change of optical properties with transport time and

471 transport height.

472           The absolute time the dust layers spent in these different height levels is presented in  
473 figure 9. We also tested the effect of relative time in relation to total transport time but could  
474 not find a clear pattern. We find a maximum value of 0.3 for  $\delta_p$  at 532 nm. On average, the  
475 depolarization decreases with increasing residence time over China. However, this  
476 dependence differs with respect to the height above ground of dust layers. The change of the  
477 depolarization ratio of dust layers travelling above 3 km above ground seems less dependent  
478 on the residence time over a given area.

479           We believe that short residence times (fast transport to Korea, 20 hours or less)  
480 reduces the chances that pollution may mix with dust, particularly if dust travelled below 3  
481 km above ground. In contrast, longer residence times (slow transport to Korea, >50 hours) of  
482 the dust plumes may have increased the chances that pollution mixed with dust if dust  
483 travelled below 3km height above ground.

484           Regarding  $\dot{A}_\beta$  we find a maximum value of 1.75 which decreases to 0.5 for slow  
485 transport of the plumes. The decrease of  $\dot{A}_\beta$  with transport time seems to be correlated for  
486 plumes that mainly stay below 3 km height above ground. In contrast, if plumes were above 3  
487 km,  $\dot{A}_\beta$  does not seem to change with transport time. In that case, the mixing of pollution with  
488 dust may have been less likely because of the fast transport.

489           With regard to  $S$  at 355 nm and 532 nm we find a maximum value of approximately  
490 75 sr which drops to approximately 40 sr for slow transport. Again, we see that for plumes  
491 below 3 km height above ground transport time seems to matter.  $S$  drops with increasing  
492 transport time. For the case of plumes above 3 km, i.e. dust that likely is not too much  
493 affected by mixing with anthropogenic pollution, the lidar ratios do not seem to depend on  
494 transport time. This result may however again be caused by the fact that transport times to  
495 Korea are comparably short.

496 We further investigated these results. We initially assumed that  $\mathring{A}_\beta$  either should  
497 increase with transport time or does not drop significantly for pollution that travels near the  
498 ground as there should be a higher share of small anthropogenic pollution particles in the dust  
499 plume (large particles). This opposite behaviour may be caused by the state of mixing, i.e.,  
500 pollution particles attach to the dust particles, thus increasing their mean size. Hygroscopic  
501 growth of particles attached to dust may further contribute to the increase of mean size. One  
502 point that complicates this interpretation is that  $\mathring{A}_\beta$  does not only depend on particle size but  
503 also on particle shape and the real and imaginary part (scattering and absorption) of the  
504 particles.

505 With regard to  $S$  we also expected that  $S$  would increase with increasing transport  
506 times. If the particles travel at low height above ground more anthropogenic pollution should  
507 mix with dust. The decrease of  $S$  however suggests an increase of particle size and a decrease  
508 of the light-absorption capacity. Hygroscopic particle growth, i.e. increase of mean particle  
509 size and decrease of light-absorption by uptake of water might be responsible for this  
510 behavior.

511 We stress that other reasons may be responsible for these results. We have a  
512 comparably small set of observations. We have insufficient information whether the plumes  
513 consisted of internal and/or external mixtures. The shape and size of particles of mixed Asian  
514 dust might be influenced in a much more significant way by transport time. The kind of  
515 mixing between the dust particles and pollution particles could influence the light-absorption  
516 properties.

517

#### 518 **4. Summary and Conclusion**

519 In this study we presented the differences of optical properties of mixed Asian dust  
520 layers in dependence of their vertical position over China during transport from the Chinese

521 dust source regions to Korea, downwind region of the source regions. The data cover the time  
522 frame from 2009-2013. The dust layers are divided into several categories which can be  
523 characterized by different heights above ground during transport. The change of height above  
524 ground during transport of the dust layers was identified by backward trajectory analysis.

525 The optical properties of Asian dust significantly change in dependence of the dust  
526 plumes, the vertical position, and the change of vertical position above ground level during  
527 transport over China. We find lower values of the lidar ratios at 355 and 532 nm, lower  
528 backscatter-related Ångström exponents (wavelength pair 355/532 nm), and higher linear  
529 particle depolarization ratios at 532 nm for Asian dust that was transported at high altitudes  
530 (> 3km height above ground) compared to the situation in which the dust plumes moved at  
531 low altitudes across China. The mean linear particle depolarization ratio is  $0.21\pm 0.06$  for  
532 transport at high altitudes. The mean lidar ratios in that case are  $52\pm 7$  sr and  $53\pm 8$  sr at 355  
533 nm and 532 nm, respectively. The mean Ångström exponent is  $0.74\pm 0.31$ . These values likely  
534 reflect properties of dust little affected by anthropogenic pollution. However, we cannot  
535 quantify the amount of anthropogenic pollution that may still be present in these dust layers.  
536 In contrast, higher values of the lidar ratios and the backscatter-related Ångström exponents,  
537 and lower values of the linear particle depolarization were found for dust layers that crossed  
538 highly polluted regions in China at low altitudes. The value of the mean linear particle  
539 depolarization ratio is  $0.13\pm 0.04$ . The mean lidar ratios are  $63\pm 9$  sr and  $62\pm 8$  sr at 355 nm  
540 and 532 nm, respectively. The mean backscatter-related Ångström exponent is  $0.98\pm 0.35$ .  
541 These values more likely describe strong influence by anthropogenic pollution, i.e. the uptake  
542 of urban pollution by dust may have been significant.

543 Our results suggest that the transport pathway as well as the vertical position of Asian  
544 dust during long-range transport may have significant impact on the optical properties of  
545 mixed Asian dust layers.

546 **Acknowledgements**

547  
548 This work was supported by a National Research Foundation of Korea (NRF) grant funded  
549 by the Korean government (MEST) (No. 2012R1A1A2002983) and the Korea  
550 Meteorological Administration Research and Development Program under grant  
551 KMIPA2015-2012.

552  
553  
554  
555  
556  
557  
558  
559  
560  
561  
562  
563  
564  
565  
566  
567  
568  
569  
570  
571  
572  
573  
574  
575  
576  
577  
578  
579  
580  
581  
582  
583  
584  
585  
586  
587  
588  
589  
590

591 **References**

592

593 Anderson, T. L., Masonis, S. J., Covert, D. S., Charlson, R. J., and Rood, M. J.: In situ  
594 measurement of the aerosol extinction-to-backscatter ratio at a polluted continental site,  
595 *Journal of Geophysical Research: Atmospheres* (1984–2012), 105, 26907-26915, 2000.

596

597 Ansmann, A., Riebesell, M., Wandinger, U., Weitkamp, C., Voss, E., Lahmann, W., and  
598 Michaelis, W.: Combined Raman elastic-backscatter lidar for vertical profiling of moisture,  
599 aerosol extinction, backscatter, and lidar ratio, *Applied Physics B*, 55, 18-28, 1992a.

600

601 Ansmann, A., Riebesell, M., and Weitkamp, C.: Measurement of atmospheric aerosol  
602 extinction profiles with a Raman lidar, *Optics Letters*, 15, 746-748, 1990.

603

604 Ansmann, A., Wandinger, U., Riebesell, M., Weitkamp, C., and Michaelis, W.: Independent  
605 measurement of extinction and backscatter profiles in cirrus clouds by using a combined  
606 Raman elastic-backscatter lidar, *Applied Optics*, 31, 7113-7131, 1992b.

607

608 Behrendt, A., and Nakamura, T.: Calculation of the calibration constant of polarization lidar  
609 and its dependency on atmospheric temperature, *Optics express*, 10, 805-817, 2002.

610

611 Bellouin, N., Quaas, J., Morcrette, J.-J., and Boucher, O.: Estimates of aerosol radiative  
612 forcing from the MACC re-analysis, *Atmospheric Chemistry and Physics*, 13, 2045-2062,  
613 2013.

614

615 Bohren, C. F., and Huffman, D. R.: Absorption and scattering by a sphere, *Absorption and*  
616 *Scattering of Light by Small Particles*, 82-129, 1983.

617

618 Burton, S., Ferrare, R., Hostetler, C., Hair, J., Rogers, R., Obland, M., Butler, C., Cook, A.,  
619 Harper, D., and Froyd, K.: Aerosol classification using airborne High Spectral Resolution  
620 Lidar measurements—methodology and examples, *Atmospheric Measurement Techniques*, 5,  
621 73-98, 2012.

622

623 Burton, S., Ferrare, R., Vaughan, M., Omar, A., Rogers, R., Hostetler, C., and Hair, J.:  
624 Aerosol classification from airborne HSRL and comparisons with the CALIPSO vertical  
625 feature mask, *Atmospheric Measurement Techniques*, 6, 1397-1412, 2013.

626

627 Burton, S., Vaughan, M., Ferrare, R., Hostetler, C.: Separating mixtures of aerosol types in  
628 airborne High Spectral Resolution Lidar data, *Atmospheric Measurement Techniques*, 7, 419-  
629 436, 2014.

630

631 Cairo, F., Di Donfrancesco, G., Adriani, A., Pulvirenti, L., and Fierli, F.: Comparison of  
632 various linear depolarization parameters measured by lidar, *Applied Optics*, 38, 4425-4432,  
633 1999.

634

635 Carrico, C. M., Kus, P., Rood, M. J., Quinn, P. K., and Bates, T. S.: Mixtures of pollution,  
636 dust, sea salt, and volcanic aerosol during ACE-Asia: radiative properties as a function of  
637 relative humidity, *J. Geophys. Res.-Atmos.*, 108(D23), 8650, doi: 10.1029/2003JD003405,  
638 2003.

639

640 Cattrall, C., Reagan, J., Thome, K., and Dubovik, O.: Variability of aerosol and spectral lidar  
641 and backscatter and extinction ratios of key aerosol types derived from selected Aerosol  
642 Robotic Network locations, *Journal of Geophysical Research: Atmospheres* (1984–2012),  
643 110, doi: 10.1029/2004JD005124, 2005.

644

645 Cesnulyte, V., Lindfors, A., Pitkänen, M., Lehtinen, K., Morcrette, J.-J., and Arola, A.:  
646 Comparing ECMWF AOD with AERONET observations at visible and UV wavelengths,  
647 *Atmospheric Chemistry and Physics*, 14, 593-608, 2014.

648

649 Chen, W.-N., Chen, Y.-W., Chou, C. C., Chang, S.-Y., Lin, P.-H., and Chen, J.-P.: Columnar  
650 optical properties of tropospheric aerosol by combined lidar and sunphotometer  
651 measurements at Taipei, Taiwan, *Atmospheric Environment*, 43, 2700-2708, 2009.

652

653 Chen, W.-N., Tsai, F.-J., Chou, C. C.-K., Chang, S.-Y., Chen, Y.-W., and Chen, J.-P.: Optical  
654 properties of Asian dusts in the free atmosphere measured by Raman lidar at Taipei, Taiwan,  
655 *Atmospheric Environment*, 41, 7698-7714, 2007.

656

657 De Tomasi, F., Blanco, A., and Perrone, M. R.: Raman lidar monitoring of extinction and  
658 backscattering of African dust layers and dust characterization, *Applied Optics*, 42, 1699-  
659 1709, 2003.

660

661 Draxler, R. R. and Rolph, G.: HYSPLIT (Hybrid Single-Particle Lagrangian Integrated  
662 Trajectory) model access via NOAA ARL READY website, NOAA Air Resources  
663 Laboratory, Silver Spring, MD, available at: <http://www.arl.noaa.gov/ready/hysplit4.html>  
664 (last access: October 2014), 2003.

665

666 Durant, A. J., Harrison, S. P., Watson, I. M., and Balkanski, Y.: Sensitivity of direct radiative  
667 forcing by mineral dust to particle characteristics, *Progress in Physical Geography*, 33, 80-  
668 102, 2009.

669

670 Eck, T., Holben, B., Reid, J., Dubovik, O., Smirnov, A., O'Neill, N., Slutsker, I., and Kinne,  
671 S.: Wavelength dependence of the optical depth of biomass burning, urban, and desert dust  
672 aerosols, *Journal of Geophysical Research: Atmospheres* (1984–2012), 104, 31333-31349,  
673 1999.

674

675 Ferrare, R. A., Turner, D. D., Brasseur, L. H., Feltz, W. F., Dubovik, O., and Tooman, T. P.:  
676 Raman lidar measurements of the aerosol extinction-to-backscatter ratio over the Southern  
677 Great Plains, *Journal of Geophysical Research: Atmospheres* (1984–2012), 106, 20333-  
678 20347, doi:10.1029/2000JD000144, 2001.

679

680 Franke, K., Ansmann, A., Müller, D., Althausen, D., Venkataraman, C., Reddy, M. S.,  
681 Wagner, F., and Scheele, R.: Optical properties of the Indo-Asian haze layer over the tropical  
682 Indian Ocean, *Journal of Geophysical Research: Atmospheres* (1984–2012), doi:  
683 10.1029/2002JD002473, 108, 2003.

684

685 Freudenthaler, V., Esselborn, M., Wiegner, M., Heese, B., Tesche, M., Ansmann, A., Müller,  
686 D., Althausen, D., Wirth, M., and Fix, A.: Depolarization ratio profiling at several  
687 wavelengths in pure Saharan dust during SAMUM 2006, *Tellus B*, 61, 165-179, 2009.

688



689 Griggs, D. J., and Noguera, M.: Climate change 2001: the scientific basis. Contribution of  
690 working group I to the third assessment report of the intergovernmental panel on climate  
691 change, *Weather*, 57, 267-269, 2002.

692

693 Huang, J., Minnis, P., Chen, B., Huang, Z., Liu, Z., Zhao, Q., Yi, Y., and Ayers, J. K.: Long-  
694 range transport and vertical structure of Asian dust from CALIPSO and surface  
695 measurements during PACDEX, *J. Geophys. Res.-Atmos.*, 113(D23), D23212, doi:  
696 10.1029/2008JD010620, 2008.

697 Huebert, B. J., Bates, T., Russell, P. B., Shi, G., Kim, Y. J., Kawamura, K., Carmichael, G.,  
698 and Nakajima, T.: An overview of ACE-Asia: strategies for quantifying the relationships  
699 between Asian aerosols and their climatic impacts, *J. Geophys. Res.-Atmos.*, 108(D23), 8633,  
700 doi: 10.1029/2003JD003550, 2003.

701

702 Husar, R. B., Tratt, D., Schichtel, B. A., Falke, S., Li, F., Jaffe, D., Gasso, S., Gill, T.,  
703 Laulainen, N. S., and Lu, F.: Asian dust events of April 1998, *Journal of Geophysical*  
704 *Research: Atmospheres* (1984–2012), 106, 18317-18330, 2001.

705

706 Inness, A., Baier, F., Benedetti, A., Bouarar, I., Chabrillat, S., Clark, H., Clerbaux, C.,  
707 Coheur, P., Engelen, R., and Errera, Q.: The MACC reanalysis: an 8 yr data set of  
708 atmospheric composition, *Atmos Chem Phys*, 13, 4073-4109, 2013.

709

710 Iwasaka, Y., Shibata, T., Nagatani, T., Shi, G. Y., Kim, Y., Matsuki, A., Trochkin, D.,  
711 Zhang, D., Yamada, M., and Nagatani, M.: Large depolarization ratio of free tropospheric  
712 aerosols over the Taklamakan Desert revealed by lidar measurements: Possible diffusion and  
713 transport of dust particles, *J. Geophys. Res.-Atmos.*, 108(D23), 8652, doi:  
714 10.1029/2002JD003267, 2003.

715

716 Jacobson, M. Z.: Investigating cloud absorption effects: Global absorption properties of black  
717 carbon, tar balls, and soil dust in clouds and aerosols, *Journal of Geophysical Research:*  
718 *Atmospheres* (1984–2012), 117, D06205, doi: 10.1029/2011JD017218, 2012

719

720 Mahowald, N. M., Muhs, D. R., Levis, S., Rasch, P. J., Yoshioka, M., Zender, C. S., and Luo,  
721 C.: Change in atmospheric mineral aerosols in response to climate: last glacial period,  
722 preindustrial, modern, and doubled carbon dioxide climates, *J. Geophys. Res.-Atmos.*,  
723 111(D10), D10202, doi: 10.1029/2005JD006653, 2006.

724

725 Mattis, I., Ansmann, A., Müller, D., Wandinger, U., and Althausen, D.: Dual-wavelength  
726 Raman lidar observations of the extinction-to-backscatter ratio of Saharan dust, *Geophysical*  
727 *Research Letters*, 29, 20-21-20-24, 2002.

728

729 McKendry, I., Hacker, J., Stull, R., Sakiyama, S., Mignacca, D., and Reid, K.: Long-range  
730 transport of Asian dust to the Lower Fraser Valley, British Columbia, Canada, *Journal of*  
731 *Geophysical Research: Atmospheres* (1984–2012), 106, 18361-18370, 2001.

732

733 Mikami, M., Shi, G., Uno, I., Yabuki, S., Iwasaka, Y., Yasui, M., Aoki, T., Tanaka, T.,  
734 Kurosaki, Y., and Masuda, K.: Aeolian dust experiment on climate impact: An overview of  
735 Japan–China joint project ADEC, *Global and Planetary Change*, 52, 142-172, 2006.

736

737 Müller, D., Ansmann, A., Mattis, I., Tesche, M., Wandinger, U., Althausen, D., and Pisani,

738 G.: Aerosol-type-dependent lidar ratios observed with Raman lidar, *J. Geophys. Res.-*  
739 *Atmos.*,112(D16), D16202, doi: 10.1029/2006JD008292, 2007.

740

741 Müller, D., Franke, K., Ansmann, A., Althausen, D., and Wagner, F.: Indo-Asian pollution  
742 during INDOEX: microphysical particle properties and single-scattering albedo inferred from  
743 multiwavelength lidar observations, *J. Geophys. Res.-Atmos.*, 108(D19), 4600, doi:  
744 10.1029/2003JD003538, 2003.

745

746 Müller, D., Mattis, I., Tatarov, B., Noh, Y., Shin, D., Shin, S., Lee, K., Kim, Y., and  
747 Sugimoto, N.: Mineral quartz concentration measurements of mixed mineral dust/urban haze  
748 pollution plumes over Korea with multiwavelength aerosol Raman-quartz lidar, *Geophys.*  
749 *Res. Lett.*, 37(20), L20810, doi: 10.1029/2010GL044633, 2010.

750

751 Murayama, T., Masonis, S. J., Redemann, J., Anderson, T. L., Schmid, B., Livingston, J. M.,  
752 Russell, P. B., Huebert, B., Howell, S. G., and McNaughton, C. S.: An intercomparison of  
753 lidar-derived aerosol optical properties with airborne measurements near Tokyo during  
754 ACE-Asia, *Journal of Geophysical Research: Atmospheres* (1984–2012), 108, doi:  
755 10.1029/2002JD003259, 2003.

756

757 Murayama, T., Müller, D., Wada, K., Shimizu, A., Sekiguchi, M., and Tsukamoto, T.:  
758 Characterization of Asian dust and Siberian smoke with multi-wavelength Raman lidar over  
759 Tokyo, Japan in spring 2003, *Geophys. Res. Lett.*, 31(23), L23103, doi:  
760 10.1029/2004GL021105, 2004.

761

762 Murayama, T.: Optical properties of Asian dust aerosol lofted over Tokyo observed by  
763 Raman lidar, *Lidar Remote Sensing in Atmospheric and Earth Sciences*, edited by  
764 Bissonnette, LR, Roy, G., and Vallée, G., Defence R&D Canada, Val-Bélair, 1, 331-334,  
765 2002.

766

767 Noh, Y. M., Kim, Y. J., Choi, B. C., and Murayama, T.: Aerosol lidar ratio characteristics  
768 measured by a multi-wavelength Raman lidar system at Anmyeon Island, Korea,  
769 *Atmospheric Research*, 86, 76-87, 2007.

770

771 Noh, Y. M., Kim, Y. J., and Müller, D.: Seasonal characteristics of lidar ratios measured with  
772 a Raman lidar at Gwangju, Korea in spring and autumn, *Atmospheric Environment*, 42,  
773 2208-2224, 2008.

774

775 Omar, A. H., Winker, D. M., Vaughan, M. A., Hu, Y., Trepte, C. R., Ferrare, R. A., Lee, K.-  
776 P., Hostetler, C. A., Kittaka, C., and Rogers, R. R.: The CALIPSO automated aerosol  
777 classification and lidar ratio selection algorithm, *Journal of Atmospheric and Oceanic*  
778 *Technology*, 26, 1994-2014, 2009.

779

780 Sakai, T., Shibata, T., Iwasaka, Y., Nagai, T., Nakazato, M., Matsumura, T., Ichiki, A., Kim,  
781 Y.-S., Tamura, K., and Troshkin, D.: Case study of Raman lidar measurements of Asian dust  
782 events in 2000 and 2001 at Nagoya and Tsukuba, Japan, *Atmospheric Environment*, 36,  
783 5479-5489, 2002.

784

785 Shimizu, A., Sugimoto, N., Matsui, I., Arao, K., Uno, I., Murayama, T., Kagawa, N., Aoki,  
786 K., Uchiyama, A., and Yamazaki, A.: Continuous observations of Asian dust and other

787 aerosols by polarization lidars in China and Japan during ACE-Asia, *J. Geophys. Res.-*  
788 *Atmos.*, 109(D19), D19S17, doi: 10.1029/2002JD003253, 2004.

789

790 Shin, S., Müller, D., Kim, Y., Tatarov, B., Shin, D., Seifert, P., and Noh, Y. M.: The retrieval  
791 of the Asian dust depolarization ratio in Korea with the correction of the polarization-  
792 dependent transmission, *Asia-Pacific Journal of Atmospheric Sciences*, 49, 19-25, 2013.

793

794 Sugimoto, N., and Lee, C. H.: Characteristics of dust aerosols inferred from lidar  
795 depolarization measurements at two wavelengths, *Applied Optics*, 45, 7468-7474, 2006.

796

797 Sugimoto, N., Nishizawa, T., Shimizu, A., Matsui, I., and Kobayashi, H.: Detection of  
798 internally mixed Asian dust with air pollution aerosols using a polarization optical particle  
799 counter and a polarization-sensitive two-wavelength lidar, *Journal of Quantitative*  
800 *Spectroscopy and Radiative Transfer*, 150, 107-113, 2015.

801

802 Sun, Y., Zhuang, G., Huang, K., Li, J., Wang, Q., Wang, Y., Lin, Y., Fu, J. S., Zhang, W.,  
803 and Tang, A.: Asian dust over northern China and its impact on the downstream aerosol  
804 chemistry in 2004, *J. Geophys. Res.-Atmos.*, 115(D17), D00K09, doi:  
805 10.1029/2009JD012757, 2010.

806

807 Sun, Y., Zhuang, G., Wang, Y., Zhao, X., Li, J., Wang, Z., and An, Z.: Chemical composition  
808 of dust storms in Beijing and implications for the mixing of mineral aerosol with pollution  
809 aerosol on the pathway, *J. Geophys. Res.-Atmos.*, 110(D24), D24209, doi:  
810 10.1029/2005JD006054, 2005.

811

812 Tatarov, B., Müller, D., Shin, D. H., Shin, S. K., Mattis, I., Seifert, P., Noh, Y. M., Kim, Y.,  
813 and Sugimoto, N.: Lidar measurements of Raman scattering at ultraviolet wavelength from  
814 mineral dust over East Asia, *Optics express*, 19, 1569-1581, 2011.

815

816 Tesche, M., Ansmann, A., Müller, D., Althausen, D., Engelmann, R., Freudenthaler, V., and  
817 Groß, S.: Vertically resolved separation of dust and smoke over Cape Verde using  
818 multiwavelength Raman and polarization lidars during Saharan Mineral Dust Experiment  
819 2008, *Journal of Geophysical Research: Atmospheres (1984–2012)*, 114,  
820 doi:10.1029/2009JD011862, 2009.

821

822 Tesche, M., Ansmann, A., Müller, D., Althausen, D., Mattis, I., Heese, B., Freudenthaler, V.,  
823 Wiegner, M., Esselborn, M., and Pisani, G.: Vertical profiling of Saharan dust with Raman  
824 lidars and airborne HSRL in southern Morocco during SAMUM, *Tellus B*, 61, 144-164, 2009.

825

826 Wandinger, U., and Ansmann, A.: Experimental determination of the lidar overlap profile  
827 with Raman lidar, *Applied Optics*, 41, 511-514, 2002.

828

829 Wang, Y., Zhuang, G., Tang, A., Zhang, W., Sun, Y., Wang, Z., and An, Z.: The evolution of  
830 chemical components of aerosols at five monitoring sites of China during dust storms,  
831 *Atmospheric Environment*, 41, 1091-1106, 2007.

832

833 Xie, C., Zhao, M., Wang, B., Zhong, Z., Wang, L., Liu, D., and Wang, Y.: Study of the  
834 scanning lidar on the atmospheric detection, *Journal of Quantitative Spectroscopy and*  
835 *Radiative Transfer*, 150, 114-120, 2015.

836  
837  
838  
839  
840  
841  
842  
843  
  
844  
  
845  
  
846  
  
847  
  
848  
  
849  
  
850  
  
851  
  
852  
  
853  
  
854  
  
855  
  
856  
  
857  
  
858  
  
859  
  
860  
  
861  
  
862  
  
863

Yi, B., Yang, P., and Baum, B. A.: Impact of pollution on the optical properties of trans-Pacific East Asian dust from satellite and ground-based measurements, *J. Geophys. Res. Atmos.*, 119(9), 5397-5409, doi: 10.1002/2014JD021721, 2014.

Yu, X., Cheng, T., Chen, J., and Liu, Y.: A comparison of dust properties between China continent and Korea, Japan in East Asia, *Atmospheric Environment*, 40, 5787-5797, 2006.

864 Table captions

865

866 Table 1. Summary of the linear particle depolarization ratio at 532 nm, lidar ratios, and backscatter-  
867 related Ångström exponents of Asian dust layers for each classification. Asian dust layers were  
868 classified according to (a) levels of anthropogenic pollution emission; LP denotes that Asian dust  
869 layers which are considered as less polluted and MP denotes that Asian dust layers which are  
870 considered as more polluted, (b) their vertical position at polluted region; Case I indicates Asian dust  
871 layers passed over China at high altitude ( $> 3$  km) before they arrived over Gwangju, and Case II  
872 indicates Asian dust layers were transported at low altitude ( $< 3$  km) over industrialized areas before  
873 they arrived over Gwangju, and (c) their vertical position (below 3 km or above 3 km) and level of  
874 pollution (LP or MP) when they passed over China

875

876 Table 2. Linear particle depolarization ratio at 532 nm, lidar ratios, and backscatter-related  
877 Ångström exponents of East Asian dust layers according to altitude range in which these plumes  
878 passed over polluted regions of China. Case I describes the layer from 3-4 km and above 4 km. Case  
879 II describes the layers from 0-1 km, from 1-2 km, and from 2-3 km height above ground.

880

881

882

883

884

885

886

887

888

889

890

891

892

893

894

895

896

897 Figure captions

898

899 Figure 1. Map of the desert regions (Taklimakan desert, Gobi desert, Badain Jaran desert, Ordos  
900 Desert, Inner Mongolia plateau, and Manchuria) and loess regions (Loess Plateau and Manchuria).  
901 The location of some major cities (Beijing and Shanghai) and industrialized areas of China (Hebei,  
902 Shandong, Henan, and Zhejiang province) is also shown. MRS.LEA is located in Gwangju, Korea.  
903

904 Figure 2. Measurement on 22 April 2012, 13:15-14:05 UTC. Shown are (a) the time-height cross  
905 section of the range-corrected signal and (b) the volume depolarization ratio at 532 nm. Also shown  
906 are the profiles of (c) the volume depolarization ratio and the linear particle depolarization ratio at 532  
907 nm, and (d) the lidar ratio at 355 and 532 nm and the backscatter-related Ångström exponents.  
908

909 Figure 3. Frequency distributions of optical properties of Asian dust observed between 2009 and 2013.  
910 Shown are (a,b) lidar ratios at 355 and 532 nm, (c) linear particle depolarization ratios at 532 nm, and  
911 (d) Ångström exponents for the wavelength pair 355/532 nm. The numbers in each plot indicate the  
912 mean value and its standard deviation, the median (shown in brackets), and the minimum and  
913 maximum value of each distribution.  
914

915 Figure 4. Distribution of AOD at 550 nm over East Asia retrieved from ECMWF for (a) and (e) dust,  
916 (b) and (f) organic matter, (c) and (g) black carbon, and (d) and (h) sulphate aerosol. (a) - (d) refers to  
917 8 March 2013. That day is classified as a relatively “low polluted” day over East China. (e) - (h) refers  
918 to 10 April 2011 which is classified as a comparably “highly polluted” day over East China.  
919

920 Figure 5. Scatter diagram of the linear particle depolarization at 532 nm versus (a), (d) the  
921 backscatter-related Ångström exponent (355/532 nm wavelength pair), (b), (e) the lidar ratio at 355  
922 nm and (c), (f) the lidar ratio at 532 nm. The left column (a-c) shows the optical properties of Asian  
923 dust layers considered as less polluted (LP), the right column (d-f) shows the more polluted cases.  
924

925 Figure 6. (top panel) Transport pattern of the dust plumes that originated in the desert regions and  
926 passed over industrialized/populated regions of China before arrival over the Korean peninsula.  
927 (middle panel) Vertical position of the dust layers during transport: (a) Dust layers passed over China  
928 at high altitude (Case I) (b) dust layers were transported over China through the near surface/lower  
929 troposphere (Case II). (bottom panel) Scatter diagram of the linear particle depolarization at 532 nm  
930 versus (c) the backscatter-related Ångström exponent (355/532 nm wavelength pair), and the (d), (e)  
931 lidar ratio (at 355 nm and at 532 nm) with respect to Case I and Case II. The two categories I, II are  
932 denoted by different colors. Case I is indicated by red circles. Case II is indicated by black circles.  
933

934  
935 Figure 7. Scatter diagram of the linear particle depolarization at 532 nm versus (a), (d) the  
936 backscatter-related Ångström exponent (355/532 nm wavelength pair), (b), (e) the lidar ratio at 355  
937 nm and (c), (f) the lidar ratio at 532 nm. The left column (a-c) shows the optical properties of Asian  
938 dust layers considered as less polluted (LP), the right column (d-f) shows the more polluted cases. The  
939 Asian dust layers that passed over polluted regions in China at low altitude are denoted by black  
940 circles. The Asian dust layers transported at high altitude are denoted by red squares.  
941

942 Figure 8. (top panel) (a) transport path and classification of East Asian dust layers with respect to (b)  
943 their altitude above ground when they passed over industrial regions of China. (bottom panel)  
944 transport path and corresponding altitude of Asian dust layers are distinguished by color. (black: 0 km  
945 – 1 km; green: 1 km – 2 km; purple: 2 km – 3 km; blue: 3 km – 4 km; red: above 4 km). Scatter plots

946 of the linear particle depolarization at 532 nm (dark yellow), the backscatter-related Ångström  
947 exponent (355/532 nm wavelength pair, red), the lidar ratio at 355 nm (blue), the lidar ratio at 532 nm  
948 (green) in dependence of the 5 altitude categories (c). The height of the Asian dust layers above  
949 ground is separated by vertical lines. Case I included the layers from 3 – 4 km and above 4 km. Case  
950 II includes the layers from 0 - 1 km, from 1-2 km, and from 2-3 km height above ground.

951

952 Figure 9. Scatter diagram of optical dust properties versus the time the Asian dust layers travelled over  
953 polluted regions in China. Shown are (a) the particle depolarization ratio, (b) the backscatter-related  
954 Ångström exponent (355/532 nm wavelength pair), (c) the lidar ratio at 355 nm, and (d) the lidar ratio  
955 at 532 nm with respect to their altitude above ground when they passed over industrial regions of  
956 China. The corresponding altitude of Asian dust layer are distinguished by color. (black: below 0 km;  
957 green: 1 km – 2km; purple: 2km – 3 km; blue: 3 km – 4 km; red: above 4 km)

958

959

960

961

962

963

964

965

966

967

968

969

970

971

972

973

974

975

976

977 Tables

978 [1]

Classification	Number of observed layers	$\delta_p$	S [sr]		$\dot{A}_p$	
			355 nm	532 nm		
Pollution level <sup>(a)</sup>	Less Polluted	25	0.17±0.02	57±7	55±7	0.82±0.37
	More Polluted	13	0.17±0.02	58±6	59±8	0.89±0.38
Vertical position <sup>(b)</sup>	Case I	16	0.21±0.06	52±7	53±8	0.74±0.31
	Case II	22	0.13±0.04	63±9	62±8	0.98±0.35
Pollution leve & Vertical position <sup>(c)</sup>	LP_below 3 km	12	0.13±0.03	64±9	62±8	1.00±0.38
	LP_above 3 km	13	0.21±0.05	51±8	49±9	0.65±0.20
	MP_below 3 km	8	0.13±0.04	61±10	64±7	1.09±0.30
	MP_above 3 km	5	0.24±0.05	53±5	53±2	0.58±0.14

979

980 [2]

Height of dust layer at pollution regions	Number of observed layers	$\delta_p$	S [sr]		$\dot{A}_p$	
			355nm	532nm		
<b>Case I</b>	Above 4 km	14	0.23±0.02	50±7	49±8	0.60±0.27
	3 km-4 km	1	0.20±0.04	44±2	47±7	0.67±0.29
<b>Case II</b>	2 km-3 km	7	0.13±0.02	61±7	66±5	1.11±0.47
	1 km-2 km	6	0.15±0.03	65±7	59±9	0.94±0.42
	Below 1 km	10	0.12±0.01	63±7	64±6	1.00±0.43

981

982

983

984

985

986

987

988

989

990

991

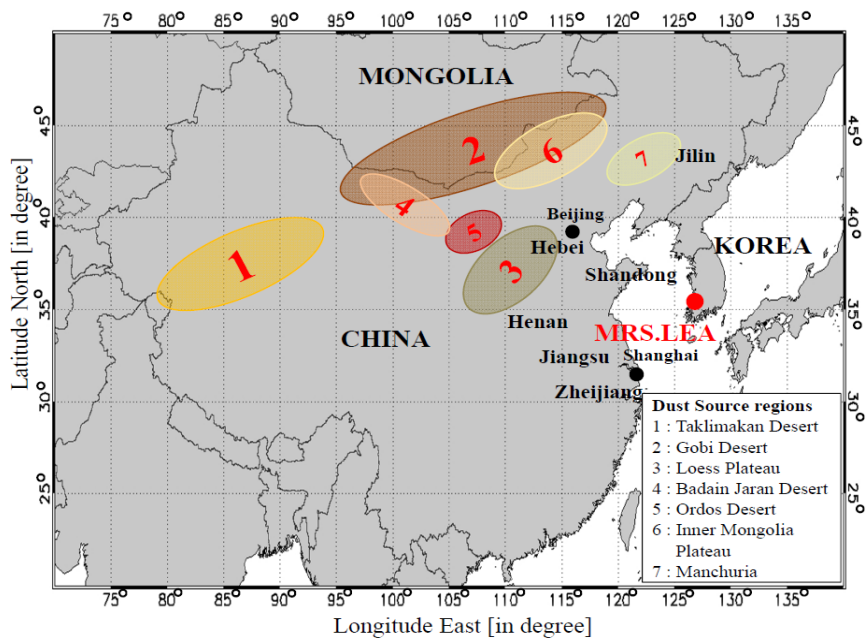
992

993



994 Figures

995 [1]



996

997

998

999

1000

1001

1002

1003

1004

1005

1006

1007

1008

1009

1010

1011 [2]

1012

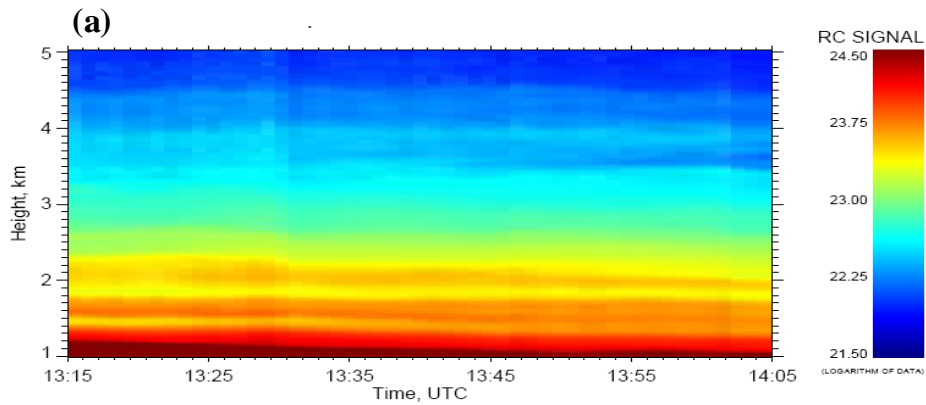
1013

1014

1015

1016

1017



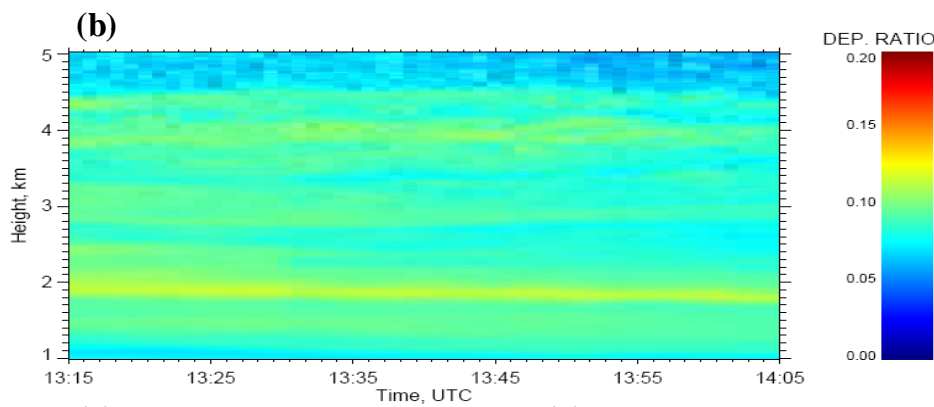
1018

1019

1020

1021

1022



1023

1024

1025

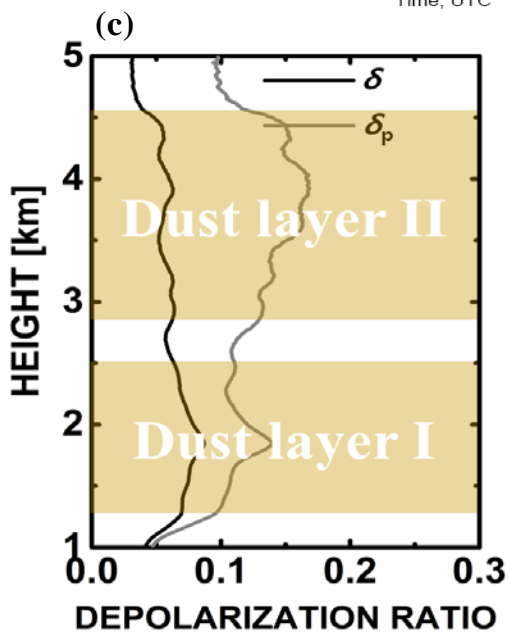
1026

1027

1028

1029

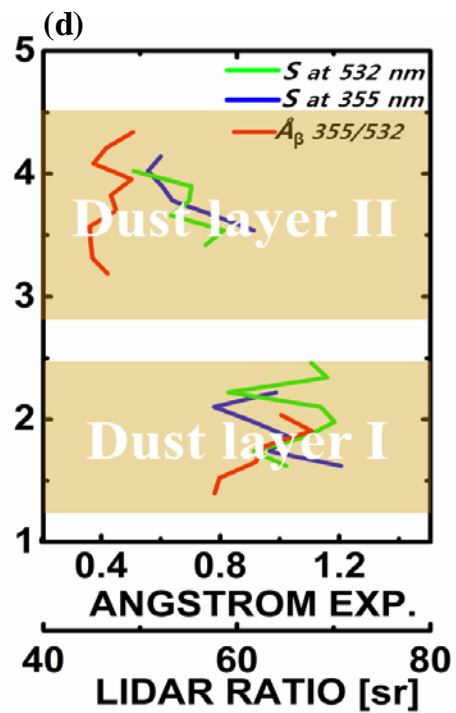
1030

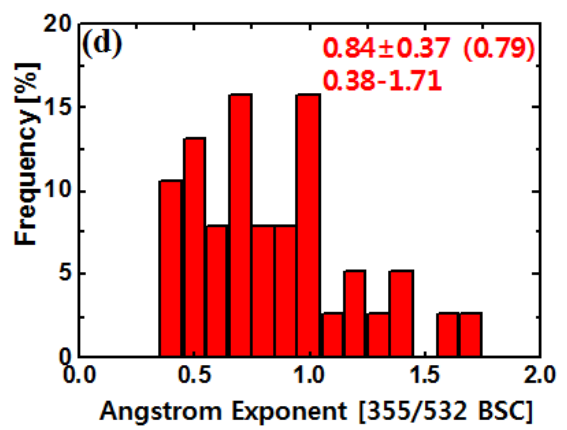
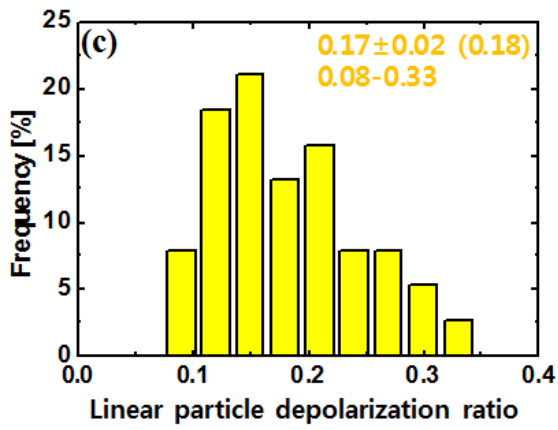
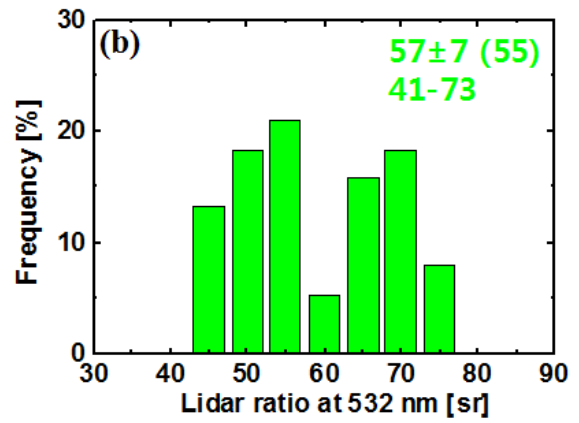
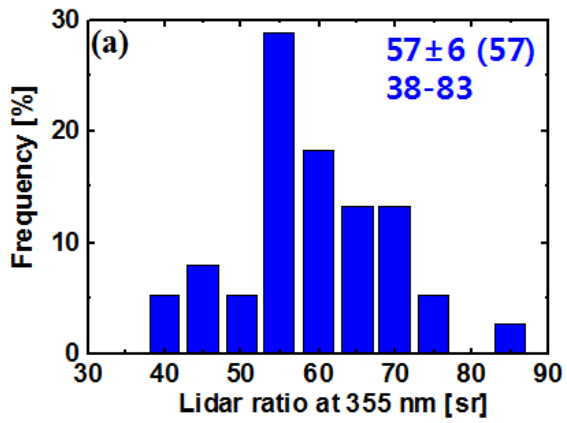


1031

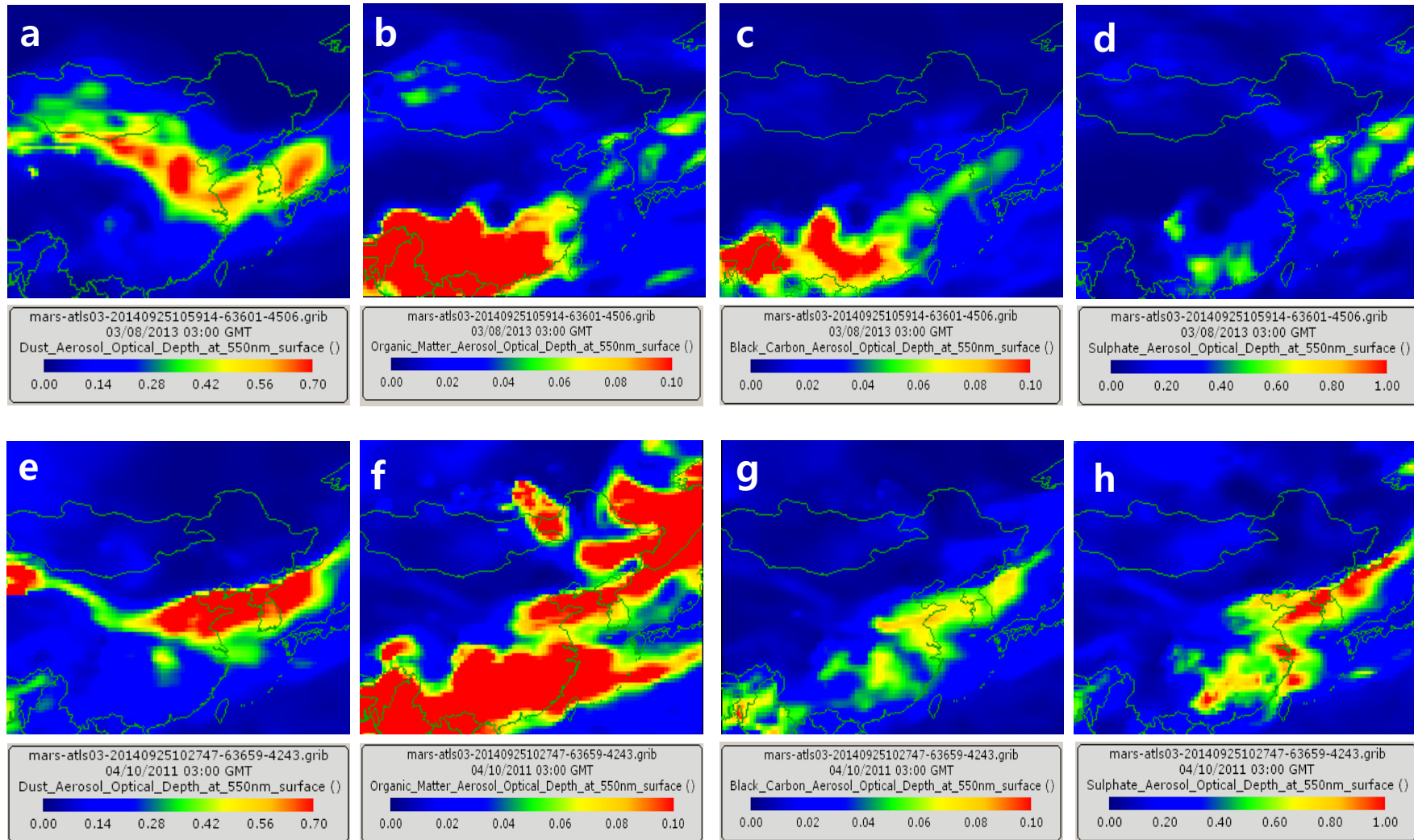
1032

1033

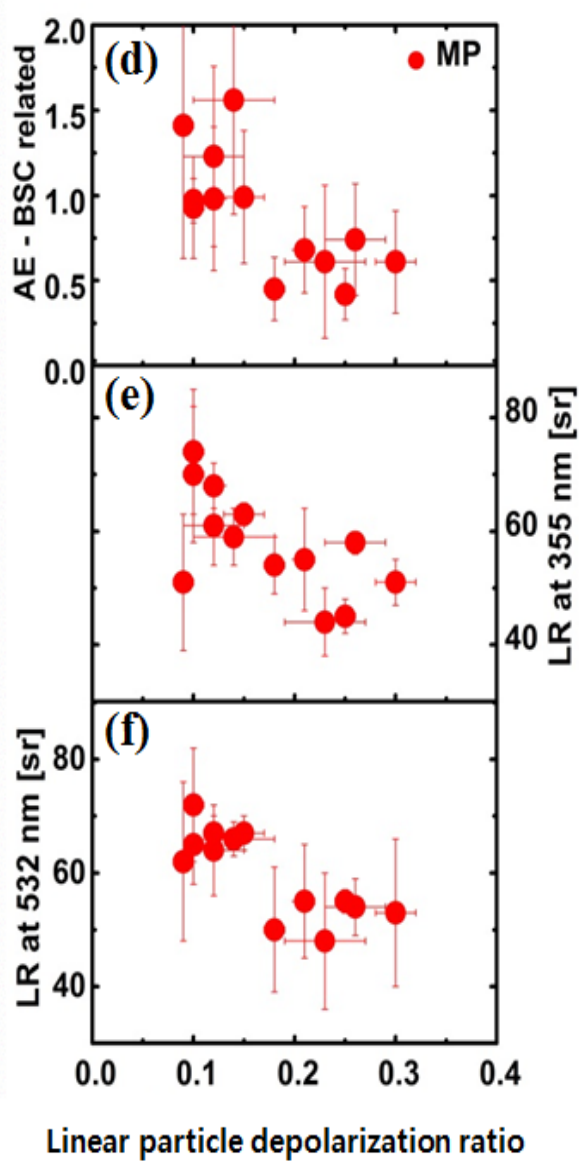
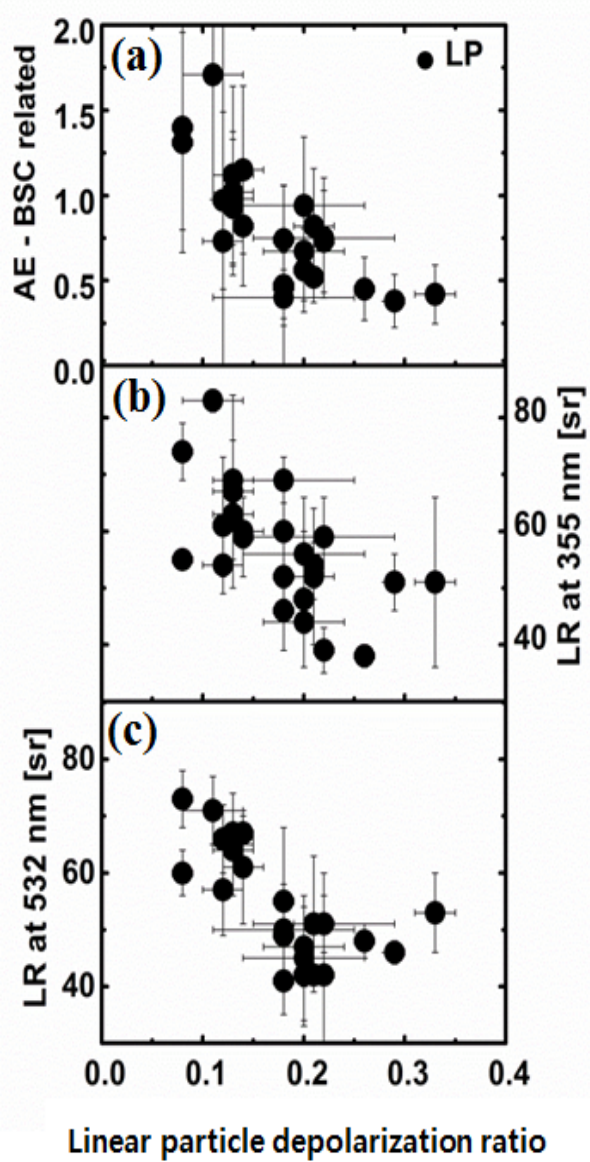




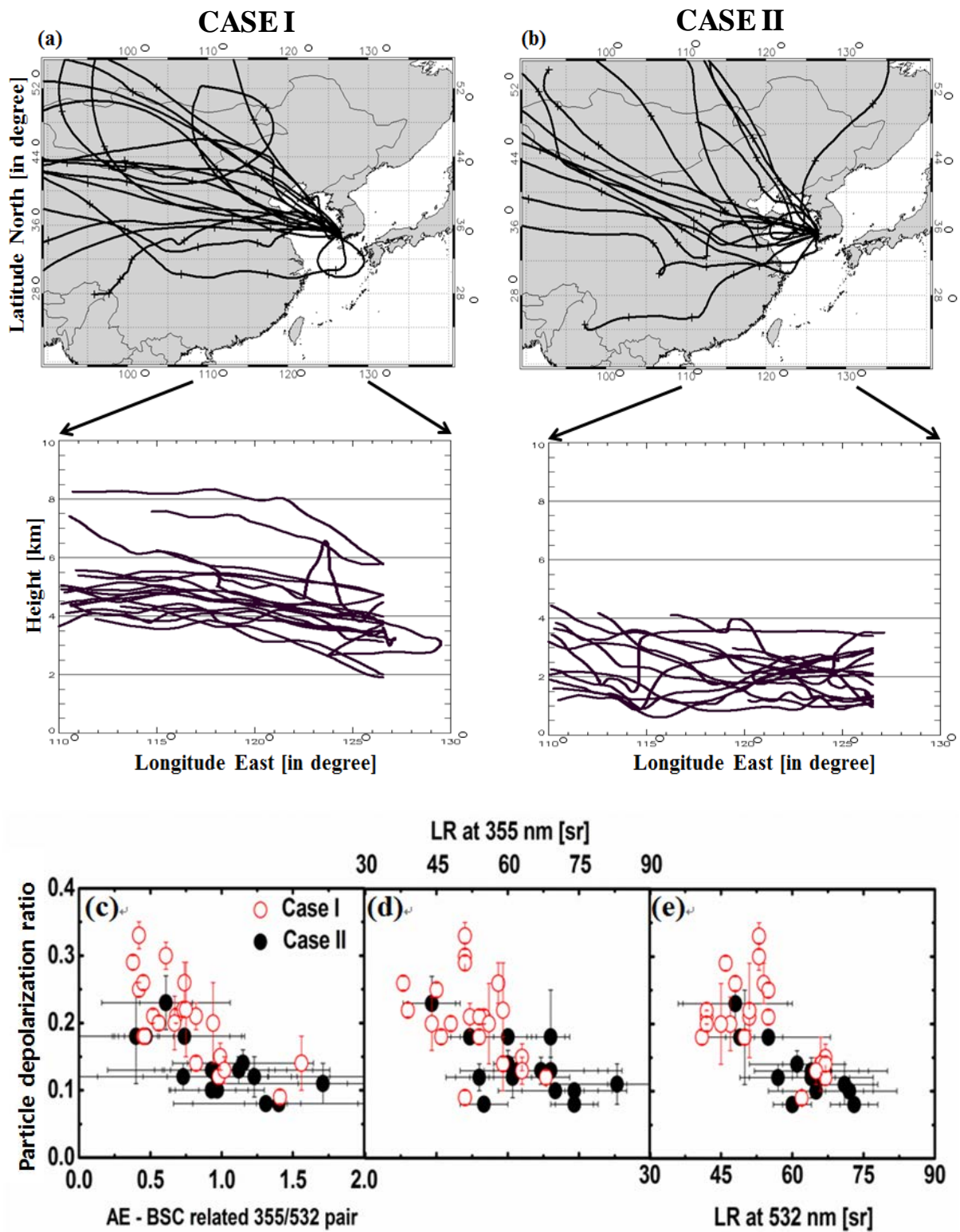
[4]



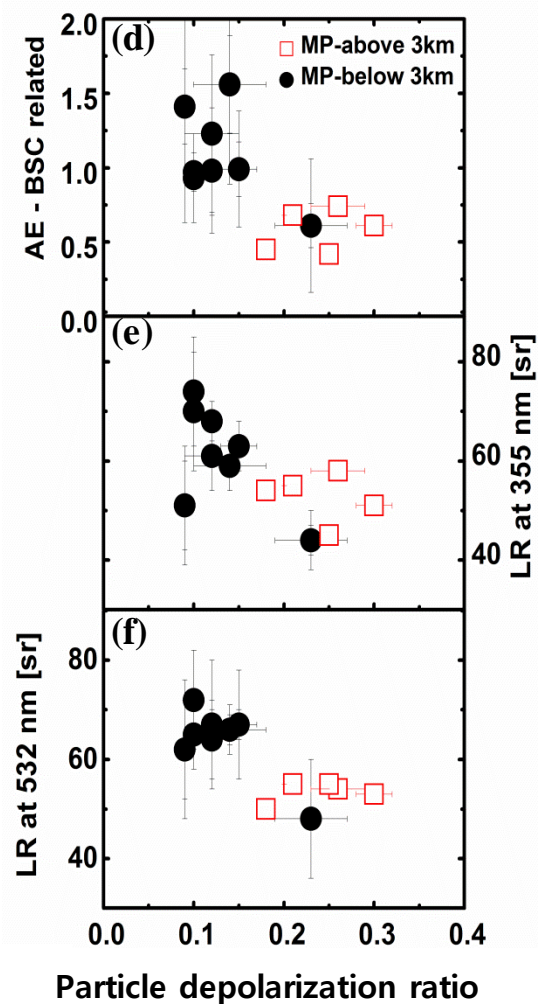
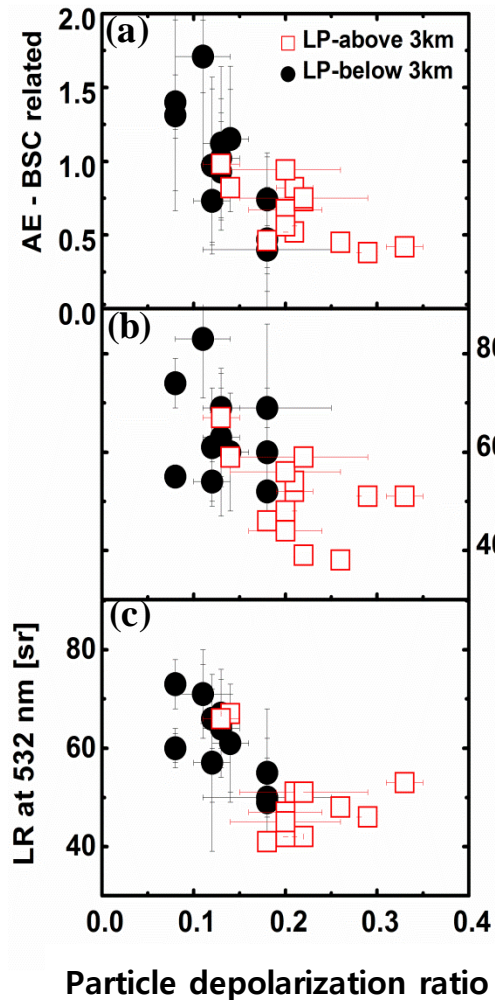
[5]



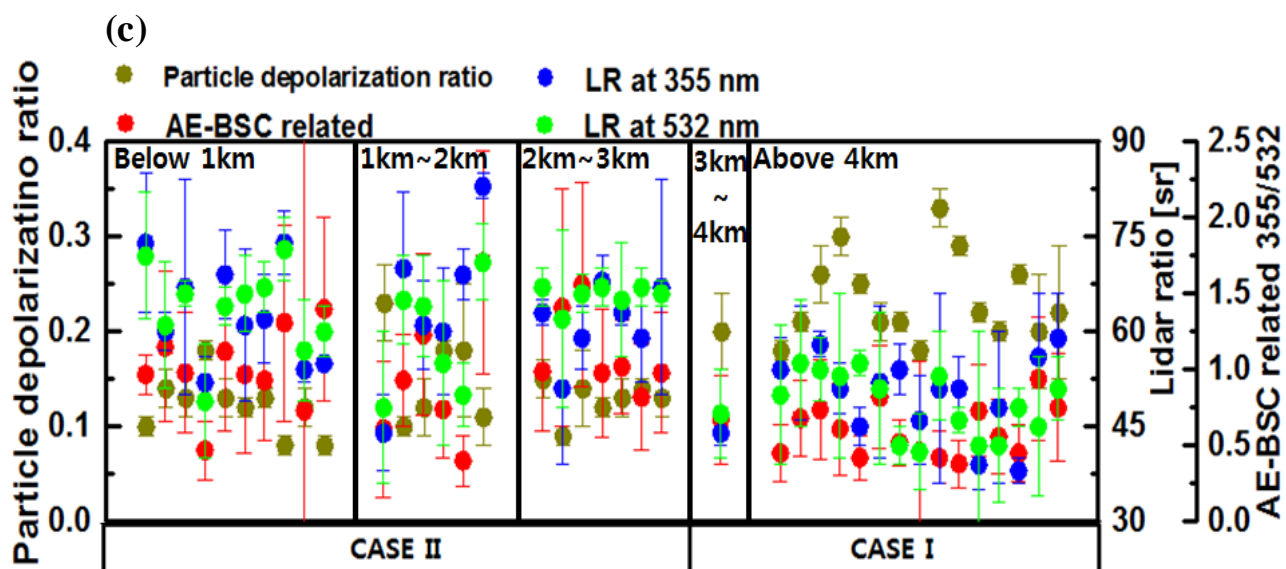
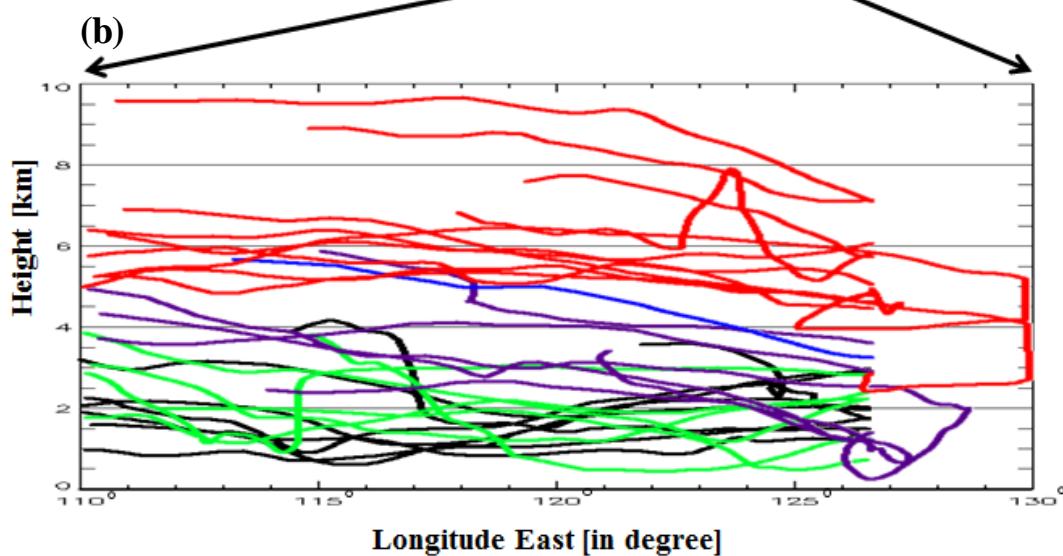
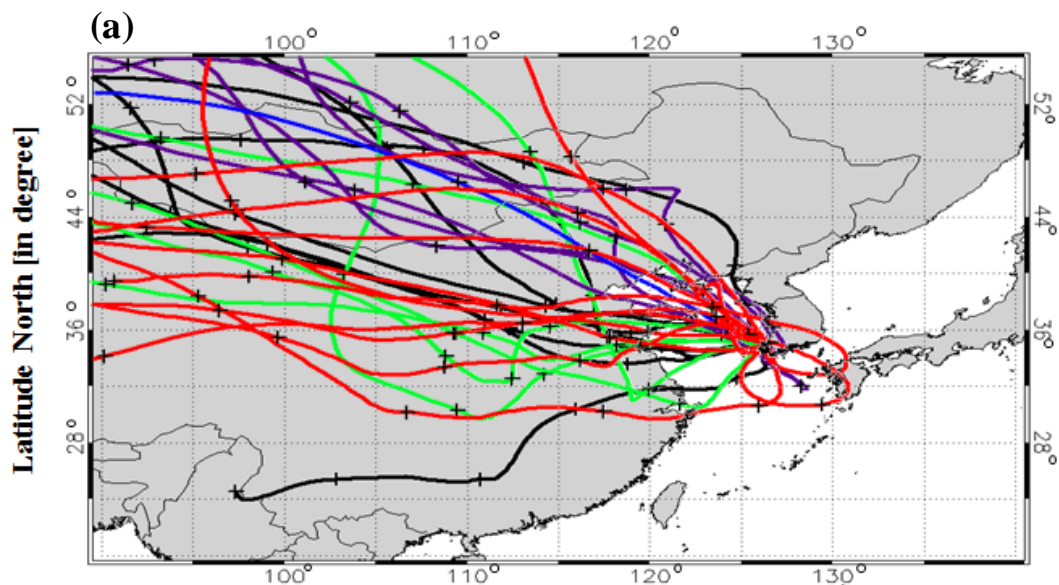
[6]







[8]





[9]

